

Joint Progressive and Coarse-to-fine Registration of Brain MRI via Deformation Field Integration and Non-Rigid Feature Fusion

Jinxin Lv, Zhiwei Wang, Hongkuan Shi, Haobo Zhang, Sheng Wang, Yilang Wang, and Qiang Li, *Member, IEEE*

arXiv:2109.12384v1 [eess.IV] 25 Sep 2021

Abstract— Registration of brain MRI images requires to solve a deformation field, which is extremely difficult in aligning intricate brain tissues, e.g., subcortical nuclei, etc. Existing efforts resort to decomposing the target deformation field into intermediate sub-fields with either tiny motions, i.e., progressive registration stage by stage, or lower resolutions, i.e., coarse-to-fine estimation of the full-size deformation field. In this paper, we argue that those efforts are not mutually exclusive, and propose a unified framework for robust brain MRI registration in both progressive and coarse-to-fine manners simultaneously. Specifically, building on a dual-encoder U-Net, the fixed-moving MRI pair is encoded and decoded into multi-scale deformation sub-fields from coarse to fine. Each decoding block contains two proposed novel modules: i) in *Deformation Field Integration (DFI)*, a single integrated sub-field is calculated, warping by which is equivalent to warping progressively by sub-fields from all previous decoding blocks, and ii) in *Non-rigid Feature Fusion (NFF)*, features of the fixed-moving pair are aligned by DFI-integrated sub-field, and then fused to predict a finer sub-field. Leveraging both DFI and NFF, the target deformation field is factorized into multi-scale sub-fields, where the coarser fields alleviate the estimate of a finer one and the finer field learns to make up those misalignments insolvable by previous coarser ones. The extensive and comprehensive experimental results on both private and public datasets demonstrate a superior registration performance of brain MRI images over progressive registration only and coarse-to-fine estimation only, with an increase by at most 10% in the average Dice.

Index Terms— Deep convolutional neural network, brain MRI registration, feature fusion, subcortical nuclei.

I. INTRODUCTION

ACCURATE registration of brain Magnetic Resonance Imaging (MRI) images allows the neurosurgeon to trace brain areas of interest, e.g., subcortical nuclei, brain functional areas, tumors, etc., across different modalities or different patients for the diagnosis of varied neurological diseases. For

Jinxin Lv, Zhiwei Wang, Hongkuan Shi, Haobo Zhang, Sheng Wang, Yilang Wang, Qiang Li are with Britton Chance Center for Biomedical Photonics, Wuhan National Laboratory for Optoelectronics and with MoE Key Laboratory for Biomedical Photonics, Collaborative Innovation Center for Biomedical Engineering, School of Engineering Sciences, Huazhong University of Science and Technology, Wuhan, Hubei 430074, China. Jinxin Lv and Zhiwei Wang are the co-first authors contributing equally to this work. Qiang Li is the corresponding author. (email:liqiang8@hust.edu.cn)

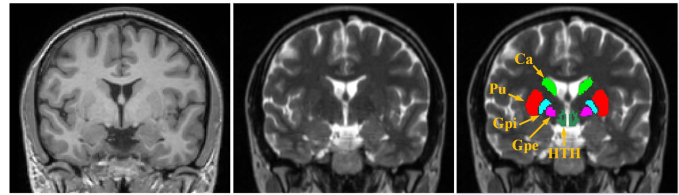


Fig. 1. From left to right: T1w image, T2w image and T2w image overlapped with ground-truth masks of subcortical nuclei.

instance, deep brain stimulation (DBS), as the most developed treatment of Parkinson’s disease, asks to electrically stimulate the subcortical nuclei of STN, GPi and GPe, which are hard to pre-locate due to blur edges, low contrasts and small scales as evidenced in Fig. 1. The most common and reliable clinical strategy is to propagate those cross-checked ground-truth masks, which were pre-defined on a MRI atlas with higher magnetic flux density, to the target MRI images via registration, namely atlas-based segmentation [1]. Similar procedure is also widely-applied to the diagnosis of Alzheimer’s disease (AD) for analyzing the changes in the volume of the hippocampus.

A deformation field, as the objective of brain MRI registration, defines a voxel-to-voxel displacement vector map from the atlas image (moving image) to the target image (fixed image) with the goal of that those same anatomical parts are spatially aligned. Traditional registration methods [2]–[10] typically search the deformation field by iteratively optimizing an empirically-formulated energy function defined by the wrapped and the fixed images. Elastix [10] proposed to deform the moving image in order to maximize its intensity-based similarity with the fixed image. ANTs [9], [11] employed the diffeomorphic transformation to estimate a deformation field which is folding-free and invertible, and thus enjoys the advantages of reversibility and topology preservation between the moved and fixed images. Despite their success, they share a common flaw of high computing cost in the optimization for medical images, not mention to high-dimensional 3D brain MRI data. It might cost minutes (by Elastix) or even hours (by ANTs) for the registration of two MRI images with the size of 160×160×160.

Recently, learning-based methods have proliferated and proposed to directly predict the deformation field in an

optimization-free inference phase. These methods usually start from establishing a parameterized mapping function from a fixed-moving image pair to its target deformation field, and then train the parameters based on a collection of unregistered pairs. Once trained, a deformation field can be obtained in no time by a single feed forward regardless of how large misalignment between the given image pair. Ground-truth deformation fields for training under the supervision are either obtained by traditional approaches, or synthesized by manual deformation transformations. For instance, Fan *et al.* [12] used the deformation field obtained by LCC-Demons [13] and SyN [9] to train a fully convolutional neural network (CNN). Zhu *et al.* [14] first randomly simulated displacement field including rotation, scale, translation and elastic deformation, and then applied it to the actual image to obtain the synthetic moving image, and finally used the generated deformation field to supervise the training of the network. However, those pseudo ground-truth deformation fields are mostly, if not all, unable to reveal the real distribution of misalignments, and thus lead to an unpromising registration performance of the supervised methods.

To address this problem, many unsupervised or weakly-supervised auxiliary constraints are designed to enhance the learning of the deformation field. Fan *et al.* [15] introduced a GAN-induced measurement as the similarity between the moved and fixed images, and forced a registration network to maximize it during the learning. Balakrishnan *et al.* [16] developed a U-Net liked framework named VoxelMorph and trained it using both volume-level similarity loss, i.e., normalized cross-correlation (NCC) or voxel-level similarity loss, i.e., mean squared error (MSE). Dalca *et al.* [17] extended the VoxelMorph, and used a probabilistic generative model to generate a diffeomorphic deformation field, well preserving the topology of the moving image. In addition to unsupervised similarities, weakly-supervised spatial coincidences of segmented areas of interest [16], [18], [19] and/or anatomical landmarks [20], [21] are also widely adopted as the training guidance of the registration methods. By benefits of those additional constraints, existing methods further push forward the registration performance, while a few efforts touch the core daunting challenge that direct estimation of the full-size deformation field is difficult on its own and hardly eased no matter how many supervisions are introduced.

In view of this, several methods attempted to alleviate the difficulty by decomposing the single deformation field into several sub-fields in either progressive manner or coarse-to-fine manner.

Progressive registration incrementally moves the moving image with a tiny motion every time, warping it onto the fixed image gradually. Volume Tweening Network (VTN) proposed by Zhao *et al.* [22] decomposed the large deformation into a series of deformation sub-fields, each of which was predicted by an independent CNN. After three times of progressively non-rigid warping, the moved image finally gets close to the fixed image. However, such decomposing is usually over-parametrized, and requires multiply cascaded stages with many isolated CNN models.

Coarse-to-fine estimation starts from predicting a lower-

resolution (coarser) deformation field where neighboring voxels are grouped and share the same displacement vector, then estimates a finer field where fewer voxels to group, and finally yields the deformation field with the same resolution of the moving image. Hu *et al.* [23] developed a dual-stream pyramid registration network (Dual-PRNet) for a coarse-to-fine estimation, which uses the last coarse field to align features of the moving and fixed images so as to help obtain the next fine field. However, Dual-PRNet only partially considers the progressive deformation, and aligns features by the last single coarse field, making the decomposition heavily fall on every two adjacent sub-fields.

In this paper, we take a further step on both works of VTN and Dual-PRNet, and propose a unified framework for robust brain MRI registration in both progressive and coarse-to-fine manners simultaneously. Our motivation is based on an argument that more light-weight CNNs or even CNN layers, i.e., decoding blocks in our implementation, could be competent in the decomposition of the full-size deformation field if the coarse-to-fine estimation is also taken into consideration. That is to say, previous layers focus on predicting coarser fields to warp features progressively so as to help estimate the next finer field. To this end, we employ a dual-encoder U-Net [24] to first encode hierarchical feature maps of the moving and fixed images separately. As shown in Fig. 2, the two feature maps at the last encoding layer are then fused and decoded into multi-scale deformation sub-fields sequentially. In each decoding block, DFI first up-scales all previous coarser sub-field(s) to the same size, and then integrates them into a single deformation field, warping by which is equivalent to warping progressively by its constituent sub-fields. Then NFF utilizes the integrated field to “progressively” deform the skip-connected encoding feature map of the moving image, and fuses the aligned moving-fixed encoding feature maps and the previous decoding feature map to obtain the next decoding feature map. Finally, the NFF-fused feature map is convolved and transformed to a finer deformation sub-field which learns to solve those misalignments remaining by all previous coarser sub-fields.

To summarize, our key contributions are as follows:

- We propose a unified framework for a robust registration of brain MRI by decomposing the single difficult deformation field in both progressive and coarse-to-fine manners jointly.
- We propose two novel modules named Deformation Field Integration (DFI) and Non-rigid Feature Fusion (NFF) to decompose the full-size deformation field in all decoding blocks instead of just two adjacent layers or multiple heavy-weight CNN models.
- Extensive and comprehensive experimental results on both public and private datasets demonstrate the superior registration performance of our unified framework and the effectiveness of our proposed two modules, i.e., DFI and NFF.

II. METHOD

Fig. 2 illustrates our unified framework, each decoding block of which consists of two major modules, i.e., Defor-

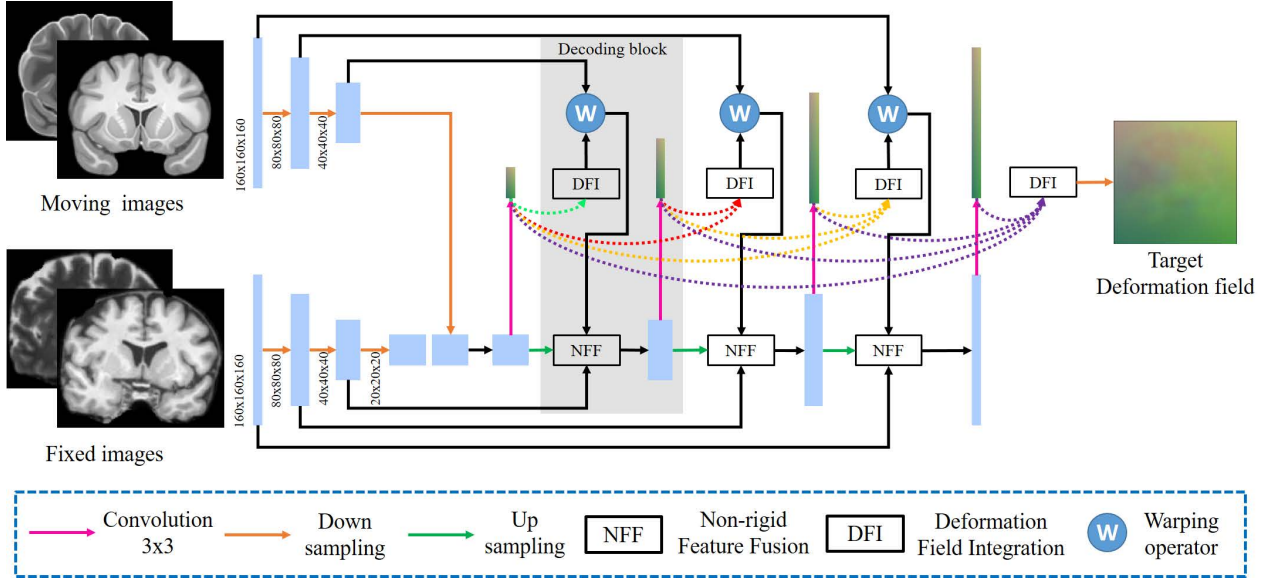


Fig. 2. The structure of the unified non-rigid registration framework, which consists of a dual-encoder U-Net backbone, and a set of DFI and NFF modules to decompose the target deformation field into multi-scale sub-fields.

mation Field Integration (DFI) and Non-rigid Feature Fusion (NFF). In the following, we first introduce the backbone of our framework, i.e., the dual-encoder U-Net (Sec. II-A), then detail both DFI and NFF (Sec. II-B&II-C), and at last give implementation and training details (Sec. II-D).

A. Unified Framework for Non-Rigid Registration

As shown in Fig. 2, the atlas and target brain MRIs are considered as moving and fixed MRIs respectively, that is, our goal is to predict a deformation field which can warp the atlas MRI onto the target MRI. Each brain MRI data consists of two modalities, i.e., T1w and T2w images which were already spatially aligned beforehand. We employ the dual-encoder U-Net [23] as our backbone, and thus directly concatenate the two (T1w and T2w) images to fit the input of the backbone. The concatenated moving images and concatenated fixed images are denoted as I_m and I_f respectively, where $I_m = \text{cat}(I_m^{T1w}, I_m^{T2w})$, $I_f = \text{cat}(I_f^{T1w}, I_f^{T2w})$, $\text{cat}(\cdot)$ means concatenation operation.

Given an unregistered pair of I_m and I_f , the dual-encoder U-Net, as its name implies, utilizes two separate encoders to extract hierarchical features from I_m and I_f respectively. Each encoding layer employs Res-blocks [25] to abstract the encoding feature map from the last layer with its resolution maintaining, and then utilizes a convolution layer with the stride equal to 2 to down-sample the abstracted map. These encoding layers derive two sets of encoding feature maps denoted as $\{E_m^{L-1}, \dots, E_m^0\}, \{E_f^{L-1}, \dots, E_f^0\}$ for I_m and I_f respectively, where E^l represents the feature map from l -th encoding layer, 0 and $L-1$ mean the deepest and the shallowest layer respectively, that is, the volume of E^l is 2^3 times larger than that of E^{l-1} , and E^{L-1} has the same size as I .

We would highlight the advantage of usage of dual-encoder comparing to the single-encoder employed in both Voxel-Morph [16] and VTN [22]. As can be seen in Fig. 2,

the discrepancy of image style between I_m and I_f is non-negligible, while the single-encoder concatenates I_m with I_f at the very first layer, which inevitably entangles both spatial misalignment and style discrepancy at those shallow layers, and embarrasses the decoder consequently. The decoder following a single-encoder not only has to reveal a deformation field from the encoded spatial misalignment, but also should keep itself from being disturbed by the entangled style discrepancy. By contrast, the dual-encoder encodes appearances of I_m and I_f separately without image style entangled, yielding encoding feature maps more friendly for the estimation of deformation map [26], [27].

We concatenate two encoding feature maps from the last layer, i.e., E_m^0 and E_f^0 , for decoding. Similar to the encoding phase, a set of decoding feature maps are obtained $\{D^0, \dots, D^{L-1}\}$, where D^l has the same size with E^l and is calculated by a decoding block except for D^0 . D^0 is obtained by directly convolving the concatenated encoding feature maps, i.e., $\text{cat}(E_m^0, E_f^0)$. Each decoding feature map goes through a convolution layer to produce a corresponding deformation sub-field, which gives a set of multi-scale deformation sub-fields denoted as $\{\phi^0, \dots, \phi^{L-1}\}$, where $\phi^l = \text{conv}(D^l)$, and the $\text{conv}(\cdot)$ represents the convolution operation which utilizes three convolutional kernels with size of $3 \times 3 \times 3$ to transform D^l to a 3-channel ϕ^l , displacement vector map for x, y, z directions.

In the following subsections, we explain how to calculate D^l in the decoding block using both DFI and NFF.

B. Deformation Field Integration Module

As shown in Fig. 3, DFI in l -th decoding block takes sub-fields from all previous blocks as inputs, and integrates them into a single field $\{\phi^0, \dots, \phi^{l-1}\} \rightarrow \Phi^l$. Fig. 3 illustrates the concrete procedure of DFI.

DFI requires all sub-fields to be up-scaled into the same size for integration. To do so, ϕ^m , where $0 \leq m < l$, is

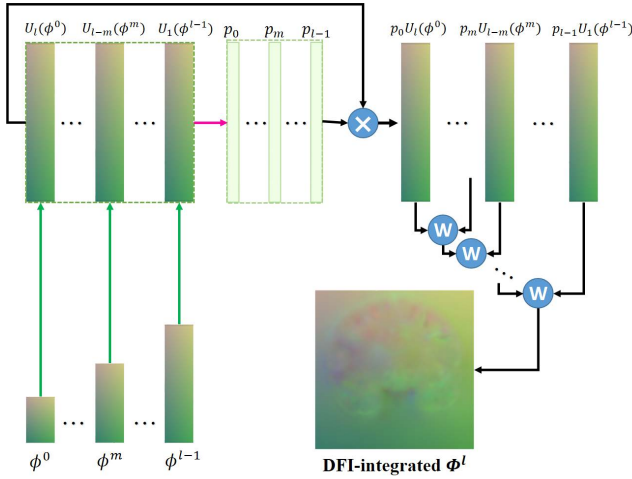


Fig. 3. The structure of DFI, which integrates sub-fields from all previous decoding blocks. The pink arrow represents the convolution operation with $3 \times 3 \times 3$ kernel size. The green arrow represents the up-sampling operation.

up-sampled by $l - m$ times, i.e., $U_{l-m}(\phi^m)$, and thus we can obtain a set of up-scaled sub-fields with the same size $\{U_l(\phi^0), \dots, U_1(\phi^{l-1})\}$. Note that confidence of the decoding block varies under different scales and different locations. Therefore, l up-scaled sub-fields are concatenated and convolved into l weighting maps $\{p_0, \dots, p_{l-1}\}$ to re-weight the contribution of each displacement vector in the corresponding sub-field, i.e., $\phi'^m = p_m U_{l-m}(\phi^m)$. To integrate them into a single deformation field Φ^l , the progressiveness should be maintained, that is, an image warped by Φ^l is the same as that warped progressively by sub-fields from ϕ'^0 to ϕ'^{l-1} as shown in Eq. (1).

$$\Phi^l \circ I = (\phi'^{l-1} \dots \circ (\phi'^1 \circ (\phi'^0 \circ I))). \quad (1)$$

According to [28], Eq. (1) can be re-written as:

$$\Phi^l = \phi'^{l-1} \dots \circ \phi'^1 \circ \phi'^0, \quad (2)$$

which implies that the integrated field Φ^l can be calculated by sequentially warping ϕ'^0 using deformation fields from ϕ'^1 to ϕ'^{l-1} as illustration in the right part of Fig. 3.

C. Non-rigid Feature Fusion module

The l -th decoding block in the dual-encoder U-Net fuses feature maps from three sources, i.e., from the two counterpart encoders (E_m^l and E_f^l) and from the last decoder (D^{l-1}). By comparing E_m^l and E_f^l , a deformation field can be inferred from the underlying hints of misalignments between fixed and moving images. This forms the basic idea of VoxelMorph [16]. However, given $\{\phi^0, \dots, \phi^{l-1}\}$ predicted by previous decoding blocks, we believe that the inference can be eased by first progressively aligning E_m^l and E_f^l instead of directly comparing them. That is, those misalignments are largely corrected by previous sub-fields beforehand, and the current decoding block can thus focus on predicting a finer sub-field ϕ^l for unsolved misalignments.

Specifically, as shown in Fig. 4, integrated field Φ^l is first used to non-rigidly transform E_m^l , i.e., $\Phi^l \circ E_m^l$. As Eq. (1)

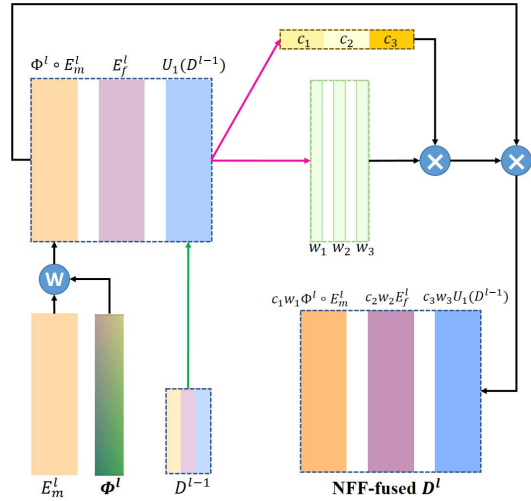


Fig. 4. The structure of NFF, which dynamically fuses features from three sources with channel and spatial attention.

and (2) implying, this process is equivalent to warping E_m^l sequentially by Φ^l 's constitution sub-fields from ϕ'^0 to ϕ'^{l-1} . Second, decoding feature map from the last block D^{l-1} is up-scaled using a transposed convolution [29] with the kernel size and the stride equal to 4 and 2 respectively, i.e., $U_1(D^{l-1})$. Third, NFF fuses the three feature maps to a new decoding feature map $\{\Phi^l \circ E_m^l, E_f^l, U_1(D^{l-1})\} \rightarrow D^l$ by both channel and spatial attentions inspired by [30].

Fig. 4 illustrates two separate branches utilized by NFF to calculate channel-wise and spatial-wise attentions respectively. One branch yields a soft-maxed attention vector c whose number of channels is the sum of the inputs'. Another branch yields three soft-maxed attention maps $\{w_1, w_2, w_3\}$. We divide c into three parts $\{c_1, c_2, c_3\}$ along channel with guarantee that $\{\Phi^l \circ E_m^l, E_f^l, U_1(D^{l-1})\}$ and $\{c_1, c_2, c_3\}$ are orderly matched with each other in terms of the channel. $\{w_1, w_2, w_3\}$ and $\{c_1, c_2, c_3\}$ are then broadcasted and multiplied together with $\{\Phi^l \circ E_m^l, E_f^l, U_1(D^{l-1})\}$ to obtain D^l as:

$$D^l = \text{cat}(c_1 w_1 \Phi^l \circ E_m^l, c_2 w_2 E_f^l, c_3 w_3 U_1(D^{l-1})). \quad (3)$$

We would highlight the differences between our method and Dual-PRNet [23] which also proposed to non-rigidly deform features for estimation. First, in Dual-PRNet features of the moving and fixed images are learned separately and interact only for prediction of deformation sub-fields, while our method utilizes NFF to fuse them as an auxiliary information to assist the prediction. Second, each sub-field in [23] is predicted based on deformed features by the last sub-field, that is, the decomposition heavily relies on the two adjacent sub-fields, while our method utilizes DFI-calculated Φ^{l-1} instead of ϕ^{l-1} to predict ϕ^l , which makes the decomposition job-shared by all l decoding blocks.

D. Implementation and Training Details

In the implementation as shown in Fig. 5, we additionally add a light-weight network on the top of the unified framework

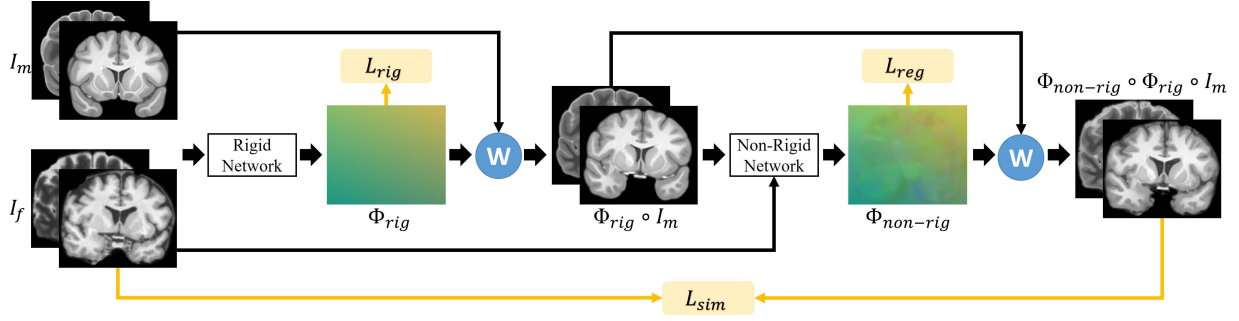


Fig. 5. The implementation of our cascaded method consisting of rigid and non-rigid parts, where the non-rigid part is our proposed unified framework.

to rigidly transform the moving image for narrowing the spatial misalignment. Both rigid and non-rigid parts can be trained in an end-to-end fashion.

I_m and I_f are first concatenated, and then the rigid network sequentially utilizes 5 Res-blocks and a fully connection layer to predict an affine transformation matrix A with the size of 3×4 (9 for rotation and 3 for translation). The affine transformation matrix is cast into a displacement vector map denoted as Φ_{rig} via spatial transform network (STN) [24], which is differentiable and allows gradients to propagate.

The rigidly moved image $\Phi_{rig} \circ I_m$, as well as I_f are fed into the following unified framework to obtain a set of deformation sub-fields $\{\phi^0, \dots, \phi^{L-1}\}$, which are integrated into the final deformation field Φ^L as presented in Sec. II-B. Here, we attribute Φ^L as $\Phi_{non-rig}$ for convenience of understanding. Therefore, the moved image can be written as $\Phi_{non-rig} \circ \Phi_{rig} \circ I_m$.

To train the cascaded rigid and non-rigid network parts, three unsupervised losses are employed as shown in Fig. 5:

1) L_{rig} for constraining Φ_{rig} : The rigid transformation loss is the same as [28].

$$L_{rig} = \left(-6 + \sum_{i=1}^3 (\lambda_i^2 + \lambda_i^{-2}) \right) + (\det(A^* + E) - 1)^2. \quad (4)$$

The first half of Eq. (4) is an orthogonality loss where $\lambda_{1,2,3}$ the singular values of $A^* + E$. And the second half of Eq. (4) is a determinant loss where A^* represents homogeneous representation of A , E is the identity matrix, and $\det(\cdot)$ is the determinant of the matrix.

2) L_{reg} for smoothness of $\Phi_{non-rig}$: Inspired by [16], we construct L_{reg} as Eq. (5) to ensure the continuity of the deformation field based on its spatial gradients:

$$L_{reg} = \frac{1}{N} \sum (\nabla_x \Phi_{non-rig})^2 + (\nabla_y \Phi_{non-rig})^2 + (\nabla_z \Phi_{non-rig})^2, \quad (5)$$

where $\nabla_x, \nabla_y, \nabla_z$ represents the difference map in x, y, z direction, and N is the total number of voxels.

3) L_{sim} for maximizing similarity between the moved and fixed image: We use Normalization Local Correlation Coefficient (NLCC) as the similarity metric, which is based on Pearson's Correlation Coefficient:

$$\rho(X, Y) = \frac{\sum (X - \bar{X})(Y - \bar{Y})}{\sqrt{\sum (X - \bar{X})^2} \sqrt{\sum (Y - \bar{Y})^2}}, \quad (6)$$

where X and Y are two variables, e.g., images.

Instead of directly calculating $\rho(\Phi_{non-rig} \circ \Phi_{rig} \circ I_m, I_f)$, we first extract multiply patches from $\Phi_{non-rig} \circ \Phi_{rig} \circ I_m$ and I_f separately using a $8 \times 8 \times 8$ sliding window with 5 voxels overlapped, and then average $-(\rho(X, Y))^2$ for those patches as L_{sim} :

$$L_{sim} = -\frac{1}{N} \sum (\rho(\Phi_{non-rig} \circ \Phi_{rig} \circ I_m^{T1w}, I_f^{T1w}, i)^2 + \rho(\Phi_{non-rig} \circ \Phi_{rig} \circ I_m^{T2w}, I_f^{T2w}, i)^2), \quad (7)$$

where $\rho(X, Y, i)$ is the ρ coefficient value for the i -th patches of X and Y .

In addition, we also employ a weakly-supervised loss namely Dice loss for better aligning those intricate brain RoIs:

4) L_{seg} for weakly-supervised guidance: The Dice [31] coefficient is a commonly adapted metric in the field of image segmentation, and is defined as :

$$Dice(X, Y) = \frac{2|X \cap Y|}{|X| + |Y|}. \quad (8)$$

The Dice loss is denoted as:

$$L_{seg} = 1 - Dice(S_f, \Phi_{non-rig} \circ \Phi_{rig} \circ S_m), \quad (9)$$

where S_f is the ground truth of fixed image I_f , S_m is the label of atlas I_m and $\Phi_{non-rig} \circ \Phi_{rig} \circ S_m$ represents the deformed atlas label.

The final loss for training can be written as:

$$L_{total} = \alpha_1 L_{rig} + \alpha_2 L_{reg} + \alpha_3 L_{sim} + \alpha_4 L_{seg}, \quad (10)$$

where the coefficients are empirically set to 0.1, 1, 1, 1 respectively. The Adam optimizer is employed to minimize Eq. (10). LeakyReLU [32] is used with slope of 0.1 as the activation function in each convolutional layer. Our method consisting of both rigid and non-rigid parts is trained for 10 epochs with the learning rate initialized as 10^{-4} , and halved after 4th epoch and after 7th epoch. The computational environment includes a software toolkit of TensorFlow [33], a GPU resource of NVIDIA RTX 3090Ti, a CPU resource of Intel Xeon Gold 5220R.

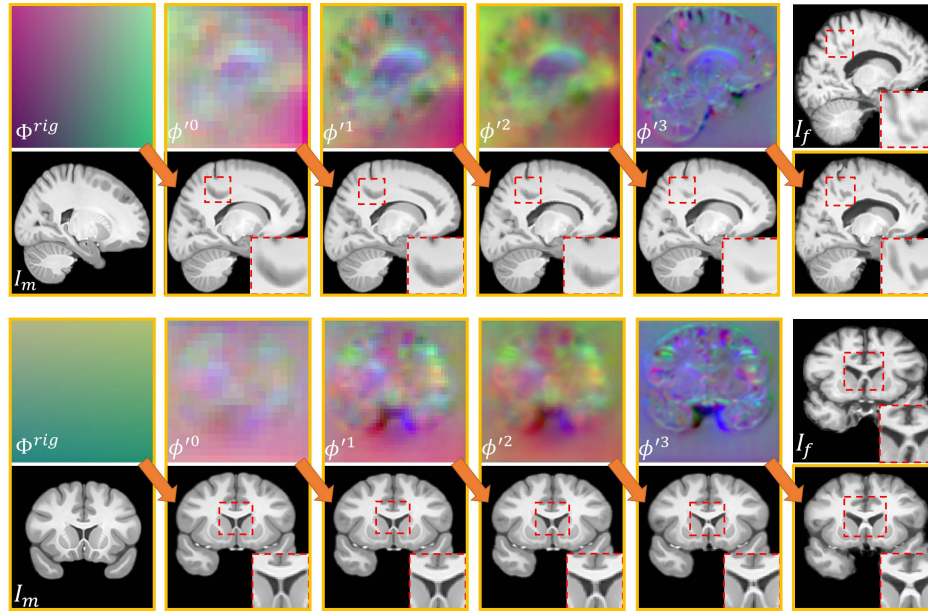


Fig. 6. Our progressive and coarse-to-fine deformation process from different views (sagittal in the first two rows and coronal in the last two rows). The sub-field on the top deforms the image (only show slice for illustration) on the bottom, yielding the moved one on the bottom-right. The fixed image is presented at the top-rightmost as the reference.

III. DATASET AND EVALUATION METRICS

A. Dataset

This study includes a private dataset and three public datasets, i.e., CIT168 atlas [34], IXI¹ and LPBA [35].

1) *CIT168 atlas*: The CIT168 atlas is a high-resolution probabilistic in-vivo anatomical atlas of subcortical nuclei. It contains two high-resolution templates with and without skull removed, each of which includes both T1w and T2w images. Masks of 16 subcortical nuclei are provided for both templates.

2) *IXI Dataset*: The IXI dataset contains 576 registered T1w and T2w MR image pairs, including 184 pairs from Hammersmith Hospital using a Philips 3T MRI system, 319 pairs from Guy's Hospital using a Philips 1.5T MRI system, and 73 pairs from Institute of Psychiatry using a GE 1.5T MRI system. Skull is removed in all data by FreeSurfer [36]. The ground-truth masks of 16 subcortical nuclei are obtained by first automatic delineation using citatlasKIT², and then manual correction by two local expert neurosurgeons.

3) *Private Dataset*: The private dataset contains 100 registered T1w and T2w MRI image pairs, which are collected using a United-Imaging 3T MRI system. Same procedure as that in the IXI dataset is performed on the private dataset to obtain the ground-truth masks.

4) *LPBA dataset*: The LPBA (LONI Probabilistic Brain Atlas) dataset contains 40 T1w images collecting from the North Shore-Long Island Jewish Health System and corresponding ground-truth masks of 56 anatomical structures. These 56 regions include 50 cortical structures, 4 subcortical areas, the brainstem, and the cerebellum. All labels were delineated by trained raters following protocols of LPBA. Skull is also removed in all data by FreeSurfer.

All data are pre-processed to crop useless black areas around the target head and to resample into the size of 128×128×128 voxels for LPBA and 160×160×160 for the rest datasets for compromising the insufficient GPU memory. Intensities are bias-corrected by ANTs [11] and linearly normalized to [0,1] by min-max normalization.

B. Evaluation Metrics

Six evaluation metrics are considered in this study, where three (i.e., NCC, MI and MSE) are unsupervised and measure the image-wise similarity, and three (i.e., Dice, HD and ASSD) require ground-truth masks to be provided. Note that values of Dice, HD and ASSD are calculated for each ROI individually and the averaged value of all ROIs are reported.

1) *Normalized cross-correlation(NCC)*: It is a commonly used similarity metric in image registration. A higher NCC indicates the two images are well-aligned. The NCC of the two images A, B is denoted as:

$$NCC(A, B) = \frac{\sum (A - \bar{A})(B - \bar{B})}{\sqrt{\sum (A - \bar{A})^2} \sqrt{\sum (B - \bar{B})^2}}.$$

2) *Mutual Information(MI)*: The MI value of the two images A, B is written as:

$$MI(A, B) = H(A) + H(B) - H(A, B),$$

where $H(A)$ and $H(B)$ represent the information entropy of image A and image B respectively, and $H(A, B)$ is the joint entropy of A and B. A higher MI indicates the two images are well-aligned.

3) *Mean Squared Error(MSE)*: The MSE value of the two images A, B is written as:

$$MSE(A, B) = \frac{1}{N} \sum |A - B|^2.$$

A lower MSE indicates the two images are well-aligned.

¹<http://brain-development.org/ixi-dataset>

²<https://github.com/jmtyszka/citatlasKIT>

TABLE I
COMPARISON RESULTS ON IXI DATASET(WEAKLY SUPERVISED)

Method	NCC	MI	MSE	Dice	HD	ASSD	Para(M)
Dual-PRNet [23]	0.958 \pm 0.005	0.547 \pm 0.007	11.983 \pm 2.602	0.702 \pm 0.136	1.276 \pm 1.454	0.314 \pm 0.166	15.03
VTN [22]	0.974 \pm 0.004	0.546 \pm 0.007	12.035 \pm 2.492	0.698 \pm 0.141	1.195 \pm 0.781	0.304 \pm 0.154	98.92
VoxelMorph [16]	0.978 \pm 0.003	0.549 \pm 0.007	11.939 \pm 2.708	0.727 \pm 0.122	1.248 \pm 1.664	0.278 \pm 0.146	14.47
Ours	0.983 \pm 0.003	0.553 \pm 0.007	11.388 \pm 2.936	0.755 \pm 0.109	1.125 \pm 1.228	0.227 \pm 0.097	15.30

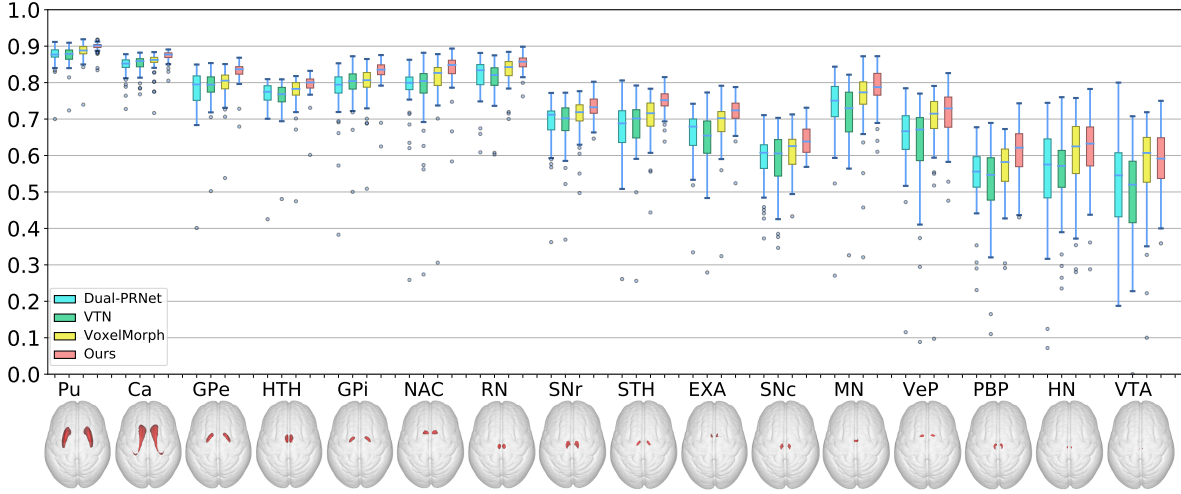


Fig. 7. Boxplots of Dice scores of 16 subcortical nuclei for comparison of methods. The subcortical nuclei phantoms are presented under the names and are ranked by the average numbers of the region voxels in decreasing order.

4) *Dice score*: The Dice score of two regions A, B is formulated as:

$$Dice(A, B) = \frac{2|A \cap B|}{|A| + |B|}.$$

The range of Dice score is from 0 to 1. When two images are registered perfectly, the Dice score is 1.

5) *Hausdorff Distance (HD)*: The Hausdorff Distance measures the maximum mismatch between surfaces of two volumes, which is formulated as:

$$HD(A, B) = \max_{a \in A} \left\{ \min_{b \in B} \{ \|a - b\| \} \right\},$$

where A and B indicate all voxels on the surfaces of two volumes respectively.

6) *Average Symmetric Surface Distance (ASSD)*: Similar to HD, ASSD measures the averaged mismatch between surfaces of two volumes, which is formulated as:

$$ASSD(A, B) = \frac{1}{|A| + |B|} \left(\sum_{a \in A} \min_{b \in B} \|a - b\| + \sum_{b \in B} \min_{a \in A} \|b - a\| \right),$$

where A and B indicate all voxels on the surfaces of two volumes respectively.

IV. EXPERIMENTAL RESULTS

A. Comparison with the state-of-the-arts on IXI

For comparison, VTN and VoxelMorph are included which have their source codes released. Dual-PRNet is also implemented and evaluated in the comparison. Note that, VTN can be treated as progressive registration only and Dual-PRNet

as coarse-to-fine estimation only. For a fair comparison, we cascade a rigid network to each comparison method which is jointly trained in an end-to-end fashion. All methods are trained by minimizing losses listed in Sec. II-D.

For evaluation, we randomly select 55 samples from IXI for testing and the rest for training. The high-quality MRI data in CIT168 is utilized as the moving image, that is, the methods are trained to register the T1w and T2w images of CIT168 to those of IXI.

Fig. 6 illustrates the visualization samples of the progressive registration process by our predicted deformation sub-fields from coarse to fine. For a better visualization, each sub-field is resized to the full size and colorized by treating x-, y-, z-direction map as red-, green-, blue-channel respectively. As can be seen, each sub-field is more detailed than the previous one. With the predicted deformation field changes from coarse to fine, the moving image deforms progressively to be more similar to the fixed image.

Table I gives the quantitative comparison results. A higher NCC, MI, Dice, and a lower MSE, HD, ASSD indicates a more accurate registration result. The best values for each column of all Table I-IV are shown in bold. From those comparison results, we can have three observations:

(1) By comparing NCC, MI and MSE values in the 2nd to 4th columns, it is demonstrated that the registered images by our method have the highest image-wise similarity than those obtained by other methods. This implies that most regions with the same anatomic semantics are well-aligned in our results.

(2) By comparing Dice, HD and ASSD values in the 5th to 7th columns, we can find that our method guarantees the most consistent RoIs, i.e., 16 subcortical nuclei, between the

TABLE II
COMPARISON RESULTS ON OUR PRIVATE DATASET(WEAKLY SUPERVISED)

Method	NCC	MI	MSE	Dice	HD	ASSD
Dual-PRNet [23]	0.966 ± 0.003	0.557 ± 0.003	10.378 ± 0.605	0.691 ± 0.135	1.474 ± 2.077	0.348 ± 0.172
VTN [22]	0.975 ± 0.002	0.558 ± 0.004	8.970 ± 0.517	0.703 ± 0.130	1.321 ± 1.692	0.319 ± 0.144
VoxelMorph [16]	0.979 ± 0.002	0.561 ± 0.004	8.250 ± 0.482	0.733 ± 0.117	1.314 ± 1.990	0.276 ± 0.133
Ours	0.984 ± 0.002	0.565 ± 0.004	7.513 ± 0.499	0.760 ± 0.098	1.070 ± 0.222	0.232 ± 0.079
VoxelMorph w/o fine-tune	0.978 ± 0.002	0.559 ± 0.004	8.523 ± 0.461	0.708 ± 0.121	1.586 ± 2.392	0.325 ± 0.161
Ours w/o fine-tune	0.983 ± 0.002	0.565 ± 0.004	7.664 ± 0.491	0.743 ± 0.109	1.196 ± 0.542	0.253 ± 0.098

TABLE III
COMPARISON RESULTS ON LPBA DATASET(UNSUPERVISED)

Method	NCC	MI	MSE	Dice	HD	ASSD
Dual-PRNet [23]	0.9880 ± 0.0030	0.6134 ± 0.0002	6.719 ± 0.836	0.706 ± 0.014	4.843 ± 0.329	1.251 ± 0.075
VoxelMorph [16]	0.9922 ± 0.0027	0.6137 ± 0.0002	5.437 ± 0.872	0.700 ± 0.015	5.000 ± 0.333	1.263 ± 0.080
VTN [22]	0.9877 ± 0.0013	0.6129 ± 0.0002	6.869 ± 0.489	0.703 ± 0.014	4.969 ± 0.333	1.286 ± 0.076
Ours	0.9945 ± 0.0028	0.6138 ± 0.0002	4.612 ± 0.954	0.721 ± 0.014	4.787 ± 0.325	1.179 ± 0.072

fixed and moved images comparing to other methods. This represents that our method can better guide the neurosurgeon to trace brain RoIs by reforming itself into an atlas-based segmentation method. Moreover, comparing with VTN and Dual-PRNet, which are progressive only and coarse-to-fine only, our proposed joint decomposition is more effective and improves the average Dice coefficient by around 8%.

(3) The last column gives the memory occupation of parameters of different methods. Our method sacrifices a little bit of computational cost comparing to Dual-PRNet and VoxelMorph (less than 1 Megabyte), but achieves the best registration performance. The usage of VTN is 7 times larger than the others' due to multi-stage strategy for decomposition, where each stage is an isolated CNN model.

Based on above three observations, it is verified that our method can improve both image-wise similarity and region-wise Dice, with a comparable requirement of computational cost to the coarse-to-fine method and more lightweight than the progressive method.

Fig. 7 shows the boxplots of the Dice scores in 16 subcortical nuclei regions obtained by different methods. As can be seen, a superior performance of registration is consistently achieved by our method except for the two smallest regions which are too challenge to reflect the performance gap between VoxelMorph and ours. However, the Dice scores obtained by our method are more stable (short length of the box) while others fluctuate as the number of region voxels decreases, verifying the robustness of our method.

B. Comparison with the state-of-the-arts on the private dataset

We examine the adaptability of comparison methods in this subsection by randomly selecting 80 samples from our private dataset for fine-tuning the models trained on the IXI dataset, and testing them on the rest 20 samples. The T1w and T2w images of CIT168 are also treated as the atlas. The comparison results are shown in 2nd to 5th rows of Table II. As can be seen, our method produces registration results with the highest image-wise similarity measured by NCC, MI and MSE, and the best consistency of RoIs evaluated by Dice, HD

and ASSD, which demonstrates a better adaptability of our method to newly collected datasets. Surprisingly, VoxelMorph is the second best among all comparison methods while it just treats the registration task as a segmentation task and employs a vanilla segmentation CNN (i.e., U-Net) without designing any interpretable module. This raises a question that *will the supervision of those RoIs contribute a lot to the high performance of segmentation-style VoxelMorph*. We answer it in the next subsection.

Moreover, to examine the generalization, we also directly applied the trained models of VoxelMorph and ours using IXI dataset, to the 20 testing samples of our private dataset without fine-tuning. For the results in 6th and 7th rows of Table II, the better performance achieved by ours presents a strong applicability of our method once trained.

C. Comparison with the state-of-the-arts on LPBA

To answer the previous question, we examine the registration performance without supervision of ground-truth ROI masks, that is, all methods are trained from scratch using the losses listed in Sec. II-D excluding L_{seg} . Since the methods are trained in an unsupervised fashion, multiple public datasets can be included. Thus, we utilize a collection of datasets including ADNI (66 T1w images) [37], ABIDE (1287 T1w images) [38], ADHD (949 T1w images) [39] for unsupervised training. In each batch, two images are randomly selected as the fixed and moving images respectively. Those trained models are evaluated on the entire LPBA with the first image as the fixed one and the rest 39 images to warp, and all evaluation metrics are reported in Table III. From those results, we find that the performance of VoxelMorph degrades and is the worst one, implying that direct usage of segmentation model could be a good “medicine” for registration but also acts as a “poison” if the supervision of RoIs is unavailable. Our method still gives the best performance comparing to the state-of-the-arts in terms of all metrics except MI.

Fig. 8 shows visual examples of the comparison results. In contrast, our deformed images are closest to the fixed one, yielding more clean subtraction images, which reflect absolute intensity differences between fixed and moved images.

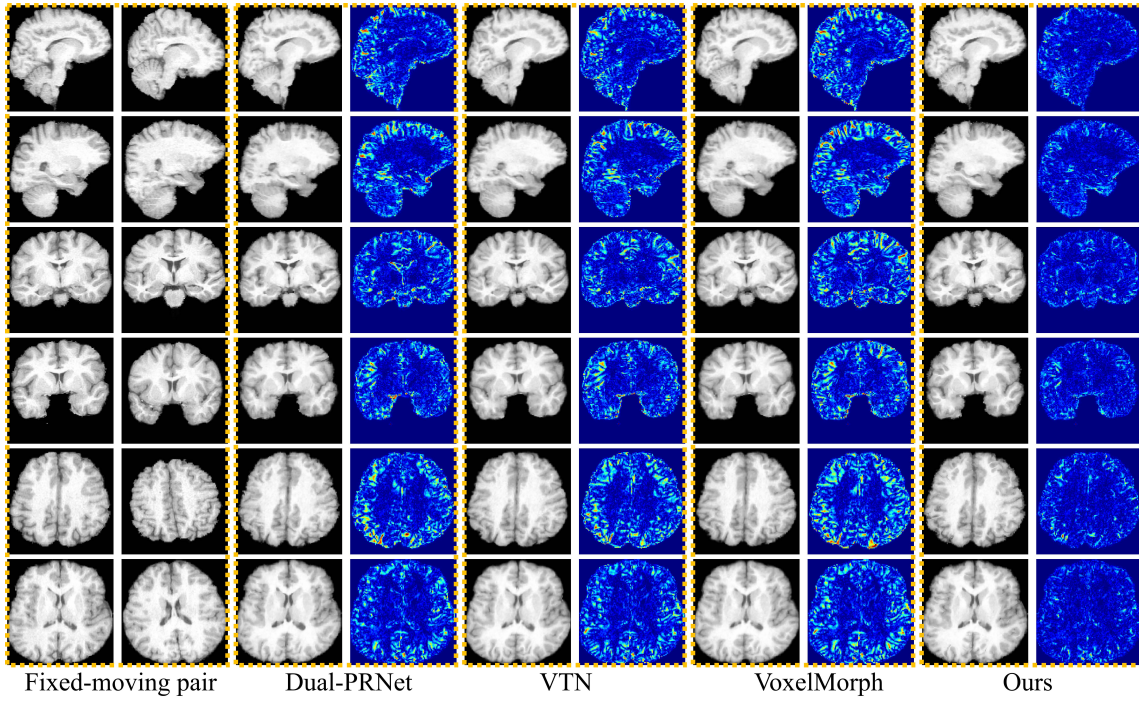


Fig. 8. From the left to right: fixed images, moving images and results obtained by comparison of methods. For each result, the moved image (left) and the subtraction image (right) are presented.

TABLE IV

RESULTS OF OUR FOUR VARIANT METHODS ON IXI DATASET. '✓' AND '-' INDICATE ENABLING AND DISABLING RESPECTIVELY.

DFI	NFF	NCC	MI	MSE	Dice	HD	ASSD
-	-	0.976 ± 0.004	0.553 ± 0.007	11.766 ± 2.710	0.714 ± 0.129	1.203 ± 1.235	0.290 ± 0.151
✓	-	0.980 ± 0.003	0.551 ± 0.007	11.661 ± 2.811	0.727 ± 0.122	1.214 ± 1.517	0.272 ± 0.130
-	✓	0.977 ± 0.004	0.552 ± 0.007	11.813 ± 2.786	0.739 ± 0.114	1.126 ± 1.098	0.254 ± 0.116
✓	✓	0.982 ± 0.003	0.553 ± 0.007	11.388 ± 2.936	0.755 ± 0.109	1.125 ± 1.228	0.227 ± 0.097

D. Ablation Studies

In this subsection, we aim at evaluating the effectiveness of our proposed two key modules, i.e., DFI and NFF. We develop four versions of our method which are trained with disabling DFI and/or disabling NFF. Specifically, with disabling DFI, those sub-fields are integrated as they are without being reweighted. With disabling NFF, feature maps from three sources are fused as they are without channel-wise and spatial-wise attentions. The ablation study is conducted based on the IXI dataset and the T1w and T2w images of CIT168 are utilized as the atlas. Table IV shows the registration results of the four versions of our method.

By comparing the first row of Table IV and the results in Table I, we can find that even without reweighting and attention, our method achieves a superior performance over VTN and Dual-PRNet, which again demonstrates the effectiveness of joint decomposition. DFI with reweighting boosts the Dice by 1.8% (see the 1st and 2nd rows) and NFF with attention improves the Dice by 3.5% (see the 1st and 3rd rows), which implies that a proper feature fusion plays an important role. Combining both modules, the Dice further increases by 3.9% and 2.2% respectively, verifying that DFI and NFF are not mutually excluded and can positively affect each other during the learning.

V. CONCLUSION

In this paper, we propose a unified framework for decomposing a target deformation field into a series of multi-scale deformation sub-fields via two novel modules, i.e., DFI and NFF. DFI dynamically integrates all previous coarser sub-fields to a single field, and NFF utilizes the integrated field to progressively align both moving and fixed encoding feature maps, and fuses the aligned feature maps and the last decoding feature map with channel and spatial attentions to help estimate a finer sub-field afterwards. DFI and NFF are used alternately and repeatedly in decoding blocks, factorizing the full-size deformation field into sub-field in both progressive and coarse-to-fine manners jointly. Comparing with progressive registration only, our method enjoys more light-weight decoding blocks instead of CNN models in separate stages, and thus makes the optimization more efficient. Comparing with the coarse-to-fine estimation only, our method splits the difficult task to those each of which a decoding block can handle rather than counting on every two adjacent layers, and thus makes the decomposition more effective. We conduct extensive and comprehensive experiments including four brain MRI datasets and three state-of-the-art registration methods. Comparison results on IXI demonstrate a superior performance of our method over other state-of-the-arts in terms of both

image-wise similarity and region-wise Dice. Experimental results on our private dataset verify the adaptability and generalization of our method. Comparison results on LPBA show the effectiveness of our joint decomposition comparing with progressive only, coarse-to-fine only and direct estimation. The ablation study also well demonstrates the significant performance gains brought by our proposed novel DFI and NFF modules. Our future work will include the extension to more modalities with huge style discrepancy, e.g., T1w and DWI, and more organs with intricate structures, e.g., small intestine.

REFERENCES

- [1] S. Ewert, A. Horn, F. Finkel, N. Li, A. A. Kühn, and T. M. Herrington, “Optimization and comparative evaluation of nonlinear deformation algorithms for atlas-based segmentation of dbs target nuclei,” *Neuroimage*, vol. 184, pp. 586–598, 2019.
- [2] M. F. Beg, M. I. Miller, A. Trouvé, and L. Younes, “Computing large deformation metric mappings via geodesic flows of diffeomorphisms,” *International journal of computer vision*, vol. 61, no. 2, pp. 139–157, 2005.
- [3] A. V. Dalca, A. Bobu, N. S. Rost, and P. Golland, “Patch-based discrete registration of clinical brain images,” in *International Workshop on Patch-based Techniques in Medical Imaging*. Springer, 2016, pp. 60–67.
- [4] B. Glocker, N. Komodakis, G. Tziritas, N. Navab, and N. Paragios, “Dense image registration through mrfs and efficient linear programming,” *Medical image analysis*, vol. 12, no. 6, pp. 731–741, 2008.
- [5] J.-P. Thirion, “Image matching as a diffusion process: an analogy with maxwell’s demons,” *Medical image analysis*, vol. 2, no. 3, pp. 243–260, 1998.
- [6] M. Zhang, R. Liao, A. V. Dalca, E. A. Turk, J. Luo, P. E. Grant, and P. Golland, “Frequency diffeomorphisms for efficient image registration,” in *International conference on information processing in medical imaging*. Springer, 2017, pp. 559–570.
- [7] X. Pennec, P. Cachier, and N. Ayache, “Understanding the “demon’s algorithm”: 3d non-rigid registration by gradient descent,” in *International Conference on Medical Image Computing and Computer-Assisted Intervention*. Springer, 1999, pp. 597–605.
- [8] T. Vercauteren, X. Pennec, A. Perchant, and N. Ayache, “Diffeomorphic demons: Efficient non-parametric image registration,” *NeuroImage*, vol. 45, no. 1, pp. S61–S72, 2009.
- [9] B. B. Avants, C. L. Epstein, M. Grossman, and J. C. Gee, “Symmetric diffeomorphic image registration with cross-correlation: evaluating automated labeling of elderly and neurodegenerative brain,” *Medical image analysis*, vol. 12, no. 1, pp. 26–41, 2008.
- [10] S. Klein, M. Staring, K. Murphy, M. A. Viergever, and J. P. Pluim, “Elastix: a toolbox for intensity-based medical image registration,” *IEEE transactions on medical imaging*, vol. 29, no. 1, pp. 196–205, 2009.
- [11] B. B. Avants, N. Tustison, and G. Song, “Advanced normalization tools (ants),” *Insight j.*, vol. 2, no. 365, pp. 1–35, 2009.
- [12] J. Fan, X. Cao, P.-T. Yap, and D. Shen, “Birnet: Brain image registration using dual-supervised fully convolutional networks,” *Medical image analysis*, vol. 54, pp. 193–206, 2019.
- [13] M. Lorenzi, N. Ayache, G. B. Frisoni, X. Pennec, A. D. N. I. (ADNI *et al.*), “Lcc-demons: a robust and accurate symmetric diffeomorphic registration algorithm,” *NeuroImage*, vol. 81, pp. 470–483, 2013.
- [14] W. Zhu, A. Myronenko, Z. Xu, W. Li, H. Roth, Y. Huang, F. Milletari, and D. Xu, “Neurreg: Neural registration and its application to image segmentation,” in *Proceedings of the IEEE/CVF Winter Conference on Applications of Computer Vision*, 2020, pp. 3617–3626.
- [15] J. Fan, X. Cao, Z. Xue, P.-T. Yap, and D. Shen, “Adversarial similarity network for evaluating image alignment in deep learning based registration,” in *International Conference on Medical Image Computing and Computer-Assisted Intervention*. Springer, 2018, pp. 739–746.
- [16] G. Balakrishnan, A. Zhao, M. R. Sabuncu, J. Guttag, and A. V. Dalca, “Voxelmorph: a learning framework for deformable medical image registration,” *IEEE transactions on medical imaging*, vol. 38, no. 8, pp. 1788–1800, 2019.
- [17] A. V. Dalca, G. Balakrishnan, J. Guttag, and M. R. Sabuncu, “Unsupervised learning of probabilistic diffeomorphic registration for images and surfaces,” *Medical image analysis*, vol. 57, pp. 226–236, 2019.
- [18] Y. Hu, M. Modat, E. Gibson, W. Li, N. Ghavami, E. Bonmati, G. Wang, S. Bandula, C. M. Moore, M. Emberton *et al.*, “Weakly-supervised convolutional neural networks for multimodal image registration,” *Medical image analysis*, vol. 49, pp. 1–13, 2018.
- [19] Z. Xu and M. Niethammer, “Deepatlas: Joint semi-supervised learning of image registration and segmentation,” in *International Conference on Medical Image Computing and Computer-Assisted Intervention*. Springer, 2019, pp. 420–429.
- [20] X. Zhong, S. Bayer, N. Ravikumar, N. Strobel, A. Birkhold, M. Kowarschik, R. Fahrig, and A. Maier, “Resolve intraoperative brain shift as imitation game,” in *Simulation, Image Processing, and Ultrasound Systems for Assisted Diagnosis and Navigation*. Springer, 2018, pp. 129–137.
- [21] M. Liu, J. Zhang, C. Lian, and D. Shen, “Weakly supervised deep learning for brain disease prognosis using mri and incomplete clinical scores,” *IEEE transactions on cybernetics*, vol. 50, no. 7, pp. 3381–3392, 2019.
- [22] S. Zhao, T. Lau, J. Luo, I. Eric, C. Chang, and Y. Xu, “Unsupervised 3d end-to-end medical image registration with volume tweening network,” *IEEE journal of biomedical and health informatics*, vol. 24, no. 5, pp. 1394–1404, 2019.
- [23] X. Hu, M. Kang, W. Huang, M. R. Scott, R. Wiest, and M. Reyes, “Dual-stream pyramid registration network,” in *International Conference on Medical Image Computing and Computer-Assisted Intervention*. Springer, 2019, pp. 382–390.
- [24] M. Jaderberg, K. Simonyan, A. Zisserman, and K. Kavukcuoglu, “Spatial transformer networks,” *arXiv preprint arXiv:1506.02025*, 2015.
- [25] K. He, X. Zhang, S. Ren, and J. Sun, “Deep residual learning for image recognition,” in *Proceedings of the IEEE conference on computer vision and pattern recognition*, 2016, pp. 770–778.
- [26] R. Liu, Z. Li, Y. Zhang, X. Fan, and Z. Luo, “Bi-level probabilistic feature learning for deformable image registration.”
- [27] L. Sun, W. Ma, X. Ding, Y. Huang, D. Liang, and J. Paisley, “A 3d spatially weighted network for segmentation of brain tissue from mri,” *IEEE transactions on medical imaging*, vol. 39, no. 4, pp. 898–909, 2019.
- [28] S. Zhao, Y. Dong, E. I. Chang, Y. Xu *et al.*, “Recursive cascaded networks for unsupervised medical image registration,” in *Proceedings of the IEEE/CVF International Conference on Computer Vision*, 2019, pp. 10600–10610.
- [29] V. Dumoulin and F. Visin, “A guide to convolution arithmetic for deep learning,” *arXiv preprint arXiv:1603.07285*, 2016.
- [30] J. Hu, L. Shen, and G. Sun, “Squeeze-and-excitation networks,” in *Proceedings of the IEEE conference on computer vision and pattern recognition*, 2018, pp. 7132–7141.
- [31] L. R. Dice, “Measures of the amount of ecologic association between species,” *Ecology*, vol. 26, no. 3, pp. 297–302, 1945.
- [32] A. L. Maas, A. Y. Hannun, and A. Y. Ng, “Rectifier nonlinearities improve neural network acoustic models,” in *Proc. icml*, vol. 30, no. 1. Citeseer, 2013, p. 3.
- [33] M. Abadi, A. Agarwal, P. Barham, E. Brevdo, Z. Chen, C. Citro, G. S. Corrado, A. Davis, J. Dean, M. Devin *et al.*, “Tensorflow: Large-scale machine learning on heterogeneous distributed systems,” *arXiv preprint arXiv:1603.04467*, 2016.
- [34] W. M. Pauli, A. N. Nili, and J. M. Tyszka, “A high-resolution probabilistic in vivo atlas of human subcortical brain nuclei,” *Scientific data*, vol. 5, no. 1, pp. 1–13, 2018.
- [35] D. W. Shattuck, M. Mirza, V. Adisetiyo, C. Hojatkashani, G. Salamon, K. L. Narr, R. A. Poldrack, R. M. Bilder, and A. W. Toga, “Construction of a 3d probabilistic atlas of human cortical structures,” *Neuroimage*, vol. 39, no. 3, pp. 1064–1080, 2008.
- [36] B. Fischl, “Freesurfer,” *Neuroimage*, vol. 62, no. 2, pp. 774–781, 2012.
- [37] S. G. Mueller, M. W. Weiner, L. J. Thal, R. C. Petersen, C. R. Jack, W. Jagust, J. Q. Trojanowski, A. W. Toga, and L. Beckett, “Ways toward an early diagnosis in alzheimer’s disease: the alzheimer’s disease neuroimaging initiative (adni),” *Alzheimer’s & Dementia*, vol. 1, no. 1, pp. 55–66, 2005.
- [38] A. Di Martino, C.-G. Yan, Q. Li, E. Denio, F. X. Castellanos, K. Alaerts, J. S. Anderson, M. Assaf, S. Y. Bookheimer, M. Dapretto *et al.*, “The autism brain imaging data exchange: towards a large-scale evaluation of the intrinsic brain architecture in autism,” *Molecular psychiatry*, vol. 19, no. 6, pp. 659–667, 2014.
- [39] P. Bellec, C. Chu, F. Chouinard-Decorte, Y. Benhajali, D. S. Margulies, and R. C. Craddock, “The neuro bureau adhd-200 preprocessed repository,” *Neuroimage*, vol. 144, pp. 275–286, 2017.